PHYSICAL REVIEW A **88**, 023816 (2013)

Enhanced self-compression of mid-infrared laser filaments in argon

Luc Bergé, Jérémie Rolle, and Christian Köhler
CEA-DAM, DIF, 91297 Arpajon, France

(Received 7 May 2013; revised manuscript received 10 July 2013; published 12 August 2013)

We investigate the nonlinear propagation of femtosecond laser filaments created at central wavelengths between 0.8 and 8 μm in a pressurized argon gas. Attention is paid to spectral broadenings and self-compression of mid-infrared pulses. It is shown that the longer the central wavelength is, the more efficient the pulse compression is. Three key mechanisms entering the spectral dynamics, i.e., low-order-harmonic generation, four-wave mixing, and self-steepening, are discussed.

DOI: 10.1103/PhysRevA.88.023816 PACS number(s): 42.65.Jx, 32.80.Fb, 52.38.Hb, 52.25.Os

I. INTRODUCTION

For a few years, the possibility to produce light filaments in gases at long pump wavelengths has raised increasing interest, from both the theoretical side [1–5] and the experimental side [6–9]. Laser filamentation proceeds from the nonlinear balance between Kerr self-focusing and defocusing by an electron plasma. On the one hand, numerical simulations predicted that the supercontinuum spanned by filaments increases with the central wavelength [1,2]. Longer wavelengths promote spatially broader filaments [4], better phase-matching conditions for harmonic generation, and more efficient self-steepening [2]. On the other hand, energetic laser sources delivering femtosecond pulses centered at mid-infrared (MIR) wavelengths are now available. Fuji and Suzuki [6] produced an ultrabroadband MIR coherent radiation by four-wave mixing (4WM) through filamentation in air, resulting in pulses of 1.3 optical cycles at $\lambda_0 = 3$ μm (λ_0 is the central wavelength of the carrier wave). Later, Chalus *et al.* [7] generated 67-fs pulses centered at 3.2 μm by means of optical parametric chirped pulse amplification techniques. Similar pulses were later used to report a 3.3-octave spectrum and tenfold compression rates in bulk crystals [10]. The first multiple-millijoule, few-cycle ($\sim$80 fs) MIR source operating at 3.9 μm [8] allowed filamentation experiments in pressurized argon [9], which emphasized supercontinua over more than three octaves.

MIR laser sources are now attracting wide interest from different physical horizons, gathering far-infrared spectroscopy, terahertz (THz) generators at relativistic laser intensities, and production of ultrahigh harmonics [11,12]. High peak intensities ($\geqslant$100 TW/cm^2) and sharp light field gradients, which can be reached in MIR filaments, initiate broad supercontinua from UV down to the THz frequency range. MIR filaments are expected to overcome important shortcomings of near-infrared pulses. In particular, they can easily reach far-infrared spectral signatures of molecular rovibrational transitions and noticeably augment laser-plasma-driven THz yields [13]. Last but not least, by widely increasing the frequency cutoff ($\sim\lambda_0^{1.7}$) along the process of high-order-harmonic generation while preserving coherence between harmonics, MIR filaments are able to produce x-ray (>1 keV) sources of a few tens of attoseconds, which opens very promising perspectives in the probing of ultrafast-electron dynamics [14,15].

Despite the previous studies, there is still a lack of knowledge about the generic behaviors of few-cycle pulses filamenting at MIR wavelengths. Therefore, the present work numerically examines the filamentation of few-cycle laser pulses centered at distinct wavelengths covering one entire decade, from 0.8 to 8 μm. Emphasis is put on spectral broadenings and capabilities of self-compression in argon. We show that better compression rates are achieved by using longer central wavelengths.

This paper is organized as follows: Section II briefly recalls our propagation equations. Section III examines the filamentation of pulses centered at near-infrared or MIR wavelengths and self-compressing in various propagation geometries and for different pulse durations. Compression performances are discussed in Sec. IV in terms of spectral broadenings. Section V validates our propagation model by comparing simulation results with data published in Ref. [9]. We finally propose to reach better compression rates by adapting appropriately the setup used in that reference.

II. THE PROPAGATION MODEL

We numerically simulate linearly polarized pulses by means of the unidirectional propagation model [16–18],

$$\partial_z \widehat{E} = \frac{i}{2k(\omega)}\nabla_\perp^2 \widehat{E} + ik(\omega)\widehat{E} + i\frac{\mu_0\omega^2}{2k(\omega)}\widehat{\mathcal{P}}_{\rm NL}, \tag{1}$$

where $\widehat{E} = \widehat{E}(x,y,z,\omega)$ denotes the Fourier transform of the electric field with respect to time. μ_0 is the vacuum permeability, $k(\omega) = \omega n(\omega)/c$ denotes the electric field wave number depending on the frequency ω, $n(\omega)$ is the refractive index of argon taken from Ref. [19], and c is the velocity of light in vacuum. The nonlinear polarization

$$\widehat{\mathcal{P}}_{\rm NL} = \widehat{P}_{\rm Kerr} + i\widehat{J}_e/\omega + i\widehat{J}_{\rm loss}/\omega \tag{2}$$

includes the Kerr effect ($P_{\rm Kerr} \propto n_2 E^3$) with nonlinear index n_2, the electron current J_e, and related absorption current $J_{\rm loss}$. $J_e(t)$ is governed by the equation

$$\partial_t J_e + \nu_e J_e = q_e^2 E\rho_e/m_e, \tag{3}$$

where ν_e is the electron collision rate; q_e, m_e, and ρ_e denote the charge, mass, and density of the free electrons, respectively. These are created by photoionization, whose rate $W(I)$ is given by the standard Perelomov, Popov and Terent'ev (PPT) theory [20], such as

$$\partial_t \rho_e = W(I)(\rho_{\rm nt} - \rho_e) + \frac{\sigma}{U_i}\rho_e I. \tag{4}$$

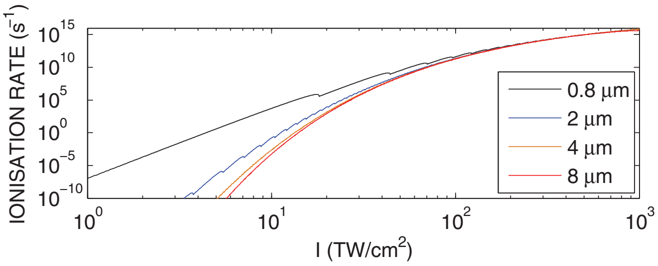

FIG. 1. (Color online) PPT ionization rates [20] vs pulse intensity in argon for different central wavelengths. From top to bottom: $\lambda_0 = 0.8$, 2, 4, and 8 μm. Ion charge and angular momentum are equal to unity.

Here, σ is the cross section for collisional ionization defined at the central frequency $\omega_0 \equiv 2\pi c/\lambda_0$, $U_i = 16$ eV is the ionization potential for argon, and $I \sim |E|^2$ is the laser intensity [18]. The photoionization rate $W(I)$ is illustrated in Fig. 1 as a function of the pulse intensity. We clearly distinguish the tunneling regime ($\gamma \ll 1$) from the multiphoton regime ($\gamma \gg 1$), fixed by the Keldysh parameter $\gamma \sim \omega_0\sqrt{2U_i/I}$. As evidenced by Fig. 1, long wavelengths drive the interaction preferentially in the tunnel ionization regime at intensities >10 TW/cm^2.

Our pulses have an initial Gaussian profile:

$$E(r,t,z=0) \sim \sqrt{\frac{P_{\text{in}}}{P_{\text{cr}}}}\, e^{-(x^2+y^2)/w_0^2 - t^2/t_p^2 - i\omega_0 t} + \text{c.c.}, \qquad (5)$$

with $1/e^2$ beam width w_0 and half extent in time t_p (c.c. means complex conjugate). $P_{\text{cr}} = \lambda_0^2/2\pi n_0 n_2(p)$ denotes the pressure-dependent critical power for self-focusing. Full-width at half-maximum (FWHM) initial pulse durations are above one optical cycle of the carrier wave, i.e., $\tau_{\text{FWHM}} \equiv \sqrt{2\ln 2}t_p > \tau_{\text{o.c.}} \equiv \lambda_0/c$. Water traces are assumed to be absent in the gas cell, and no specific resonance is expected in the considered range of infrared wavelengths.

In the coming analysis, we shall start with an initial power ratio $P_{\text{in}}/P_{\text{cr}} = 15$ at 0.8-μm wavelength in argon and for 1 bar pressure. To preserve the same initial intensity and energy when passing to longer wavelengths, we will decrease the power ratio but increase the pressure proportionally. At 2 μm, we fix this ratio to $P_{\text{in}}/P_{\text{cr}} = 5.8$ with $p = 2.5$ bars, while at 4 μm, $P_{\text{in}}/P_{\text{cr}} = 2.9$ with $p = 5$ bars. Anticipated upon further technological developments, pulses operating at a 8-μm central wavelength will also be examined, and they will logically involve a halved power ratio, $P_{\text{in}}/P_{\text{cr}} = 1.45$, for a doubled pressure $p = 10$ bars. Kerr index coefficients will be chosen within a narrow value interval: At 0.8 μm we shall opt for the well-known nonlinear index $n_2 = p \times 10^{-19}$ cm^2/W [21–23]. For $\lambda_0 \geqslant 2$ μm, the Kerr index n_2 will have values close to $0.97p \times 10^{-19}$ cm^2/W, as proposed in [24].

By doing so, the collisional cross section σ, starting from 1×10^{-19} cm^2, is expected to increase as $\nu_c/\omega_0^2 \sim p\lambda_0^2$. In contrast, chromatic dispersion does not change as much when keeping the ratio p/λ_0 constant. Group-velocity dispersion (GVD) indeed remains normal [25] for $0.8 \leqslant \lambda_0 \leqslant 8$ μm, and it prevails over higher-order dispersive terms. The variations of its characteristic coefficient $k'' \equiv \partial^2 k/\partial\omega^2|_{\omega=\omega_0}$ are then almost exactly compensated by the pressure increase, i.e., $k'' \simeq 0.2 \times (p/1\text{ bar})(0.8/\lambda_0\,[\mu\text{m}])$ fs^2/cm, valid at all investigated wavelengths. The GVD strength $\sim w_{\text{fil}}^2 k''/\lambda_0$, in contrast, decreases at comparable filament width w_{fil}.

Equations (1)–(4) are numerically integrated by means of a split-step scheme in radially symmetric geometry for which the transverse Laplacian of Eq. (1) reduces to $\nabla_\perp^2 = r^{-1}\partial_r r \partial_r$ with $r = \sqrt{x^2+y^2}$. The code exploits a finite-difference (Crank-Nicholson) scheme in r and is spectral in time. Chromatic dispersion is treated in the Fourier domain, while the nonlinear terms (Kerr effect, plasma coupling terms, and losses) are integrated in real space between two steps of linear propagation. The increment Δz is adaptive and evaluated at each step from the pulse nonlinear phase. Parallelization employs message-passing interface architecture. Typical spatiotemporal steps are $\Delta r = 4.4$ μm, $\Delta t \simeq 0.1$ fs while $\Delta z \leqslant 0.3$ μm.

III. MIR FILAMENTS IN COLLIMATED AND FOCUSED PROPAGATION GEOMETRIES

To start with, the top row of Fig. 2 displays the dynamics of different Gaussian pulses operating at $\lambda_0 = 0.8$, 2, and 4 μm (from left to right), with $w_0 = 750$ μm, $t_p = 20$ fs, and no linear focusing. At 0.8 μm, the input power is 15 times critical for a local pressure of $p = 1$ bar. We retrieve standard features of ultrafast laser filamentation in gases [18]: The pulse decays into multiple peaks in time, located in the leading or trailing edge of the pulse. When increasing λ_0, the power ratio is diminished, which decreases the number of focusing-defocusing events. As expected, comparable filamentary structures undergo less dispersion. The squared modulus of the field amplitude develops oscillations whose period $\lambda_0/2c$ corresponds to the difference between the pulse central wavelength and its third harmonic generated by the Kerr response. By passing to 2 and then 4 μm, this period increases together with self-steepening [1,2]. As shown by Figs. 2(a) and 2(b), pulse compression results not from the net reduction of the wave-field oscillations but from the amplification and compression of a small number of them. The bottom row shows pulse distributions in the (r,t) plane where the shock structure induced by self-steepening helps to isolate one "hypercompressed" cell at long wavelengths (see 4-μm pulse). Minimum FWHM durations are 5.3 fs at 2 μm and 4.7 fs at 4 μm. In the latter case, the cross-correlation frequency-resolved optical gating (XFROG) trace evidences that the compressed peak is associated with the buildup of shorter wavelengths ($\sim$0.64 μm); i.e., self-compression is achieved in the visible part of the supercontinuum.

Similar properties are retrieved in focused geometry. Figure 3 shows the propagation of pulses with $t_p = 40$ fs and a 3-mm beam width, focused by a lens of 1.5-m focal length and keeping all other laser parameters unchanged. When passing from 2 to 8 μm, the clamped filament intensity [Fig. 3(a)] and electron density [Fig. 3(b)] decrease to some extent with $W(I)$ (see Ref. [2]). The filament waist increases as $w_{\text{fil}} \sim \lambda_0/\sqrt{p}$, and the self-channeling range extends along comparable distances $\Delta z_{\text{fil}} \sim \lambda_0/pI_{\text{fil}}$. The energy lost by multiphoton absorption increases with λ_0 [solid curves in Fig. 3(d)], which reflects the high number of photons required to ionize Ar at MIR wavelengths. We can notice that the energy trapped inside a 300-μm radius disk around the filament core

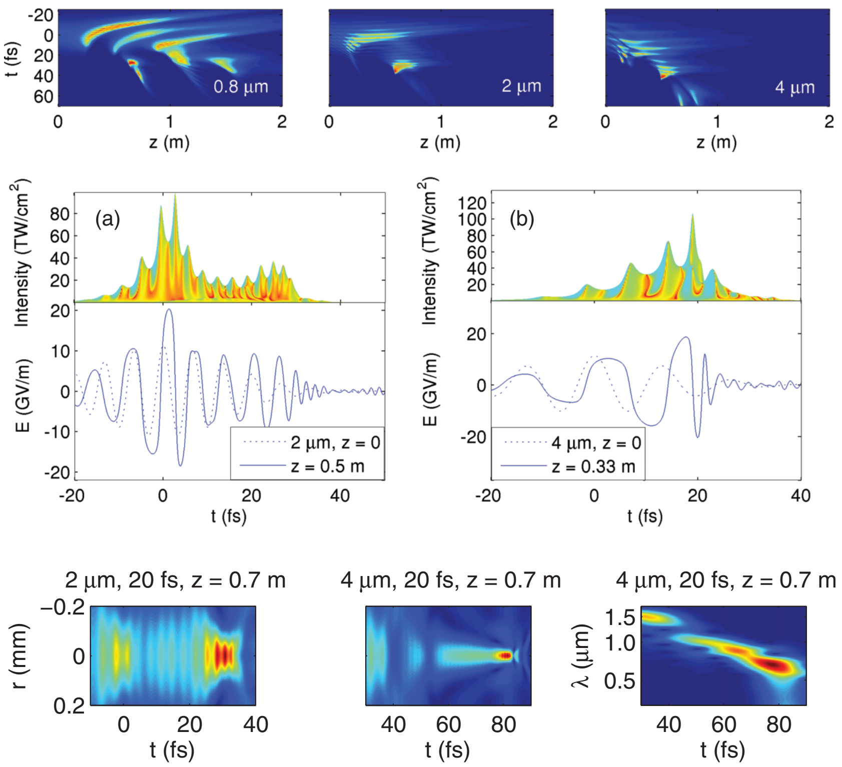

FIG. 2. (Color online) Top row: Dynamics of collimated 20-fs, 750-μm Gaussian pulses in the (t,z) plane at 0.8, 2, and 4 μm. Middle row: View of $I(r,z,t)$ vs time (top), where the intensity I is defined by the absolute square of the complex electric field, and on-axis field amplitude (bottom, solid curves) for (a) the 2-μm pulse at $z = 0.5$ m and (b) the 4-μm pulse at $z = 0.33$ m. The dotted curves recall field oscillations at $z = 0$. Bottom row: Spatiotemporal distributions at distances of maximum compression for $\lambda_0 = 2$ and 4 μm. The last subplot shows the ω-dependent XFROG trace expressed as a function of the wavelength λ for the latter pulse.

(shown by the dashed curves) keeps high levels, i.e., around 2–3 mJ. The bottom row details the (z,t) dynamics of the 2-, 4-, and 8-μm filaments. We again find a less efficient dispersion before focus ($1 \leqslant z \leqslant 1.3$ m). The main difference with collimated pulses (see the top row of Fig. 2) is the recurrent refocusing of the rear pulse after the linear focus.

Figure 4 (top) details the evolution of the FWHM pulse duration along the propagation axis. This duration decreases all the more as the central wavelength is long. More precisely, a first compression event occurs at the beginning of the filament once full plasma generation takes place and intensity clamping starts at $z \simeq 1$ m. Maximum compression is attained at this distance by the 8-μm pulse, reaching about 5-fs FWHM duration. This behavior is compatible with recent simulation results reported in [26], where the infrared ($\sim$2.2 μm) component of a two-color pulse (0.8-μm pump and 0.45-μm seed pulse), triggered by four-wave mixing, was compressed down to a single cycle at the onset of filamentation. Compression was then lost 30 cm farther. In our setup, at least two additional compression events undergone by initially MIR pulses happen at linear focus and then close to the distance $z = 1.75$ m. Interestingly, with the 8-μm pulse, a series of ultracompression

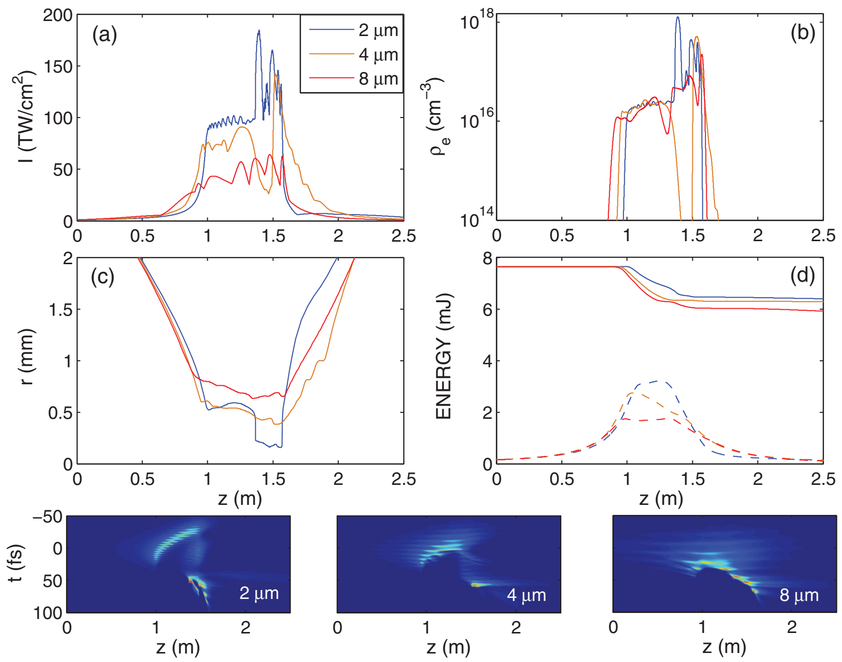

FIG. 3. (Color online) (a) Maximum intensity, (b) peak electron density, (c) beam radius, and (d) total (solid curves) and partial (dashed curves) energy loss of 40-fs, 3-mm Gaussian pulses focused with a $f = 1.5$ m lens in argon and operating at 2 μm [blue upper curve, see 3(a)], 4 μm (brown middle curve) and 8 μm (red bottom curve). In (d) the energy measurement is performed within a circle of 300 μm surrounding the filament core (dashed curves). Bottom row: Corresponding dynamics in the (z,t) plane.

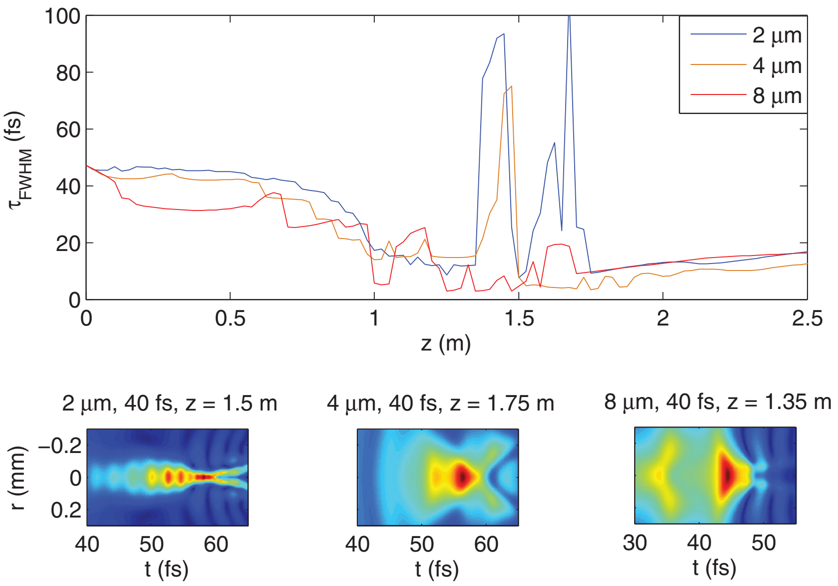

FIG. 4. (Color online) Top: FWHM pulse duration vs the propagation distance z. Bottom: Spatiotemporal distributions at distances of maximum compression.

stages occur before focus, maintaining the FWHM pulse duration at around 3 fs. Self-compression ceases once the pulse intensity drops below 10 TW/cm^2 and as the electron density reaches very low levels ($\rho_{e,\,\max} < 10^7$ cm^{-3}). We report the following records (bottom row in Fig. 4): $\tau_{\rm FWHM} = 7.6$ fs at 2 μm ($z = 1.5$ m), $\tau_{\rm FWHM} = 3.4$ fs at 4 μm ($z = 1.75$ m), and $\tau_{\rm FWHM} = 2.9$ fs at 8 μm ($z = 1.35$ m). The shortest durations survive over propagation lengths that increase with λ_0 (sometimes after the end of the filament), which we again attribute to less dispersion at long wavelengths.

IV. SUPERCONTINUUM GENERATION

Pulse compression is associated with the emergence of a broad supercontinuum. Spectral broadening follows four generic steps: First, low-order harmonics occur early, upon the linear coherence length of the third harmonic, $L_{3\omega} \equiv \pi/[k(3\omega_0) - 3k(\omega_0)]$. Typically, $L_{3\omega}$ increases from 0.17 mm at 0.8-μm wavelength to 3 mm at 8-μm wavelength, including pressure effects. Longer coherence lengths allow harmonics to be built with higher conversion efficiency. Second, the primary focusing of the leading pulse left after the first ionization front redshifts the spectrum. Fundamental and low-order harmonics broaden and provide a potential source for further redshift through 4WM (see below). Third, refocusing of the trailing pulse produces two peaks in time, whose interferences form oscillations in the spectrum [27]. Fourth, self-steepening (and plasma generation to a lesser extent) enhances the buildup of smaller wavelengths.

Figures 5(a)–5(c) display on-axis intensity spectra of the 0.8-, 2-, and 4-μm pulses with $t_p = 20$ fs at $z = 0$ (dotted curves), at the first diagnosed distance ($z = 2.5$ cm) where low-order harmonics appear (black dashed curves), and at distances of maximal spectral extent [colored (gray) solid curves]. Measured at the 10^{-2} intensity level, these spectra can span a large number of octaves, defined by $N = \ln{(\lambda_{\max}/\lambda_{\min})}/\ln 2$. N increases with the maximum wavelength $\lambda_{\max}$ excited in the infrared domain and with the minimum one $\lambda_{\min}$, fixed by both harmonic generation and self-steepening efficiency. $\lambda_{\min}$ does not vary very much with short pulses and stays, e.g., around 0.23 μm for the 20-fs pulses at all central wavelengths. The same tendency is confirmed in focused geometry [Figs. 5(d)–5(f)], where conversion into low-order harmonics is less efficient due to the longer initial pulse duration. As shown by the dash-dotted brown curve of Fig. 5(e), preventing harmonic generation limits spectral broadening to a small extent only, i.e., in the UV-visible region, which was checked to yield similar compression rates. Spectra broaden from two octaves for the 20-fs collimated pulse at 0.8 μm to five octaves for the 40-fs focused pulse at 8 μm. They clearly show the buildup of wavelengths shorter than $\lambda_0/3$, whose corresponding optical cycle remains comparable with the FWHM of the most compressed pulse.

Wavelengths excited in the far-infrared can, instead, be attributed to 4WM following the basic conversion scheme

$$\lambda_{\rm IR}^{-1} = 2\lambda_0^{-1} - \lambda_s^{-1}. \tag{6}$$

Let us indeed choose a reference IR wavelength, $\lambda_{\rm IR}^{\rm ref} = 2\lambda_0$, which must be exceeded by combining λ_0 and an active seed component with wavelength λ_S. By "active," we conjecture that this seed component should exceed 10^{-2} times the pump spectral intensity to trigger an IR component [28,29]. Then λ_S should belong to the interval $\lambda_0/2 < \lambda_S \leqslant 2\lambda_0/3$. The production of wavelengths $> \lambda_{\rm IR}^{\rm ref}$ through 4WM thus requires that the pump broadens enough to reach 66% of its initial value, which is better assured by short pulses operating at long central wavelengths. This condition is fulfilled early by MIR pulses but not by the 0.8-μm pulse. In Ref. [26] the efficiency of the 4WM mechanism for producing compressed infrared light fields was tested in the filamentation regime. It was shown that, despite distortions induced by the nonlinear propagation of the spectral components, Eq. (6), which proceeds from a fundamental energy conservation law, still holds when the seed and generated components are identified by the wavelengths maximizing their respective distributions in the pulse spectrum.

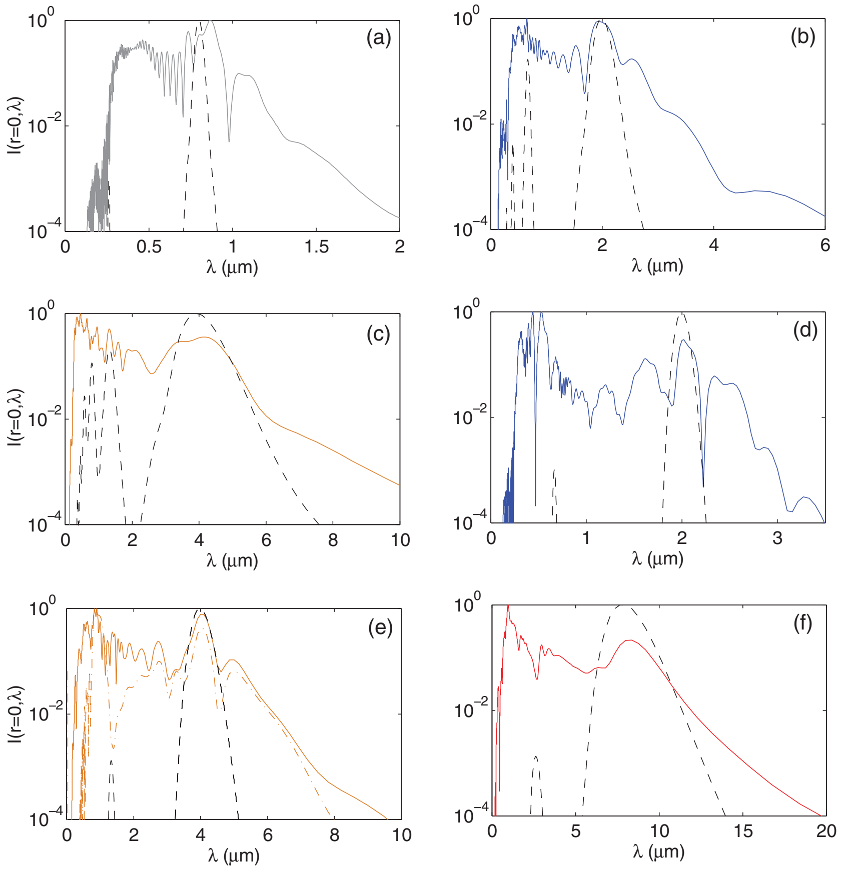

FIG. 5. (Color online) On-axis normalized intensity spectra vs wavelength for (a) $\lambda_0 = 0.8\ \mu$m, (b) $\lambda_0 = 2\ \mu$m, and (c) $\lambda_0 = 4\ \mu$m for the 20-fs collimated pulse and (d) $\lambda_0 = 2\ \mu$m, (e) $\lambda_0 = 4\ \mu$m, and (f) $\lambda_0 = 8\ \mu$m for the 40-fs focused pulse. The black dashed curves refer to the distance $z = 2.5$ cm; the colored (gray) solid curves indicate the broadest spectrum reached at (a) $z = 0.7$ m, (b) $z = 0.6$ m, (c) $z = 0.5$ m, (d) $z = 1.575$ m, (e) $z = 1.55$ m for the 4-μm, 40-fs pulse with (solid brown curve) and without harmonic generation (dash-dotted brown curve), and (f) $z = 1.575$ m for the 8-μm, 40-fs pulse. Note the changes of scales in the λ axis.

V. ENHANCING PULSE COMPRESSION

We find it worthwhile to test the possibility to generate a light structure that is a few femtoseconds long by adapting the experimental setup of Ref. [9]. To validate our model, Fig. 6 shows simulation results for the pulse parameters employed in this experiment, namely, a 3.9-μm, 6.5-mJ, 80-fs FWHM pulse with a sixth-order super-Gaussian profile in time and a Gaussian profile in space with $w_0 = 6$ mm, focused by a 2-m lens in Ar at 4.5 bars pressure. The simulation model is the one recalled in Sec. II, and it discards higher-order Kerr nonlinearities [22,30]. Figures 6(a) and 6(b) compare our numerical results (black curves) with the experimental data [pink (gray) curves] for the voltage current measured along the filament path and proportional to the plasma density (here expressed in linear scale) and for the spectra corresponding to the input pulse (dotted curves) and to the visible and infrared parts of the filament (solid curves), respectively. We multiplied each measured spectral intensity of [9] by a factor λ^2 to tune correctly our normalization constants. Also we multiplied the voltage values by the arbitrary factor 2×10^{16} to provide a direct comparison with our free-electron density. Our numerical results are in good agreement with the experimental data up to slight discrepancies in the plasma distribution and in the most infrared part of the spectrum ($\lambda > 4.5\ \mu$m). They

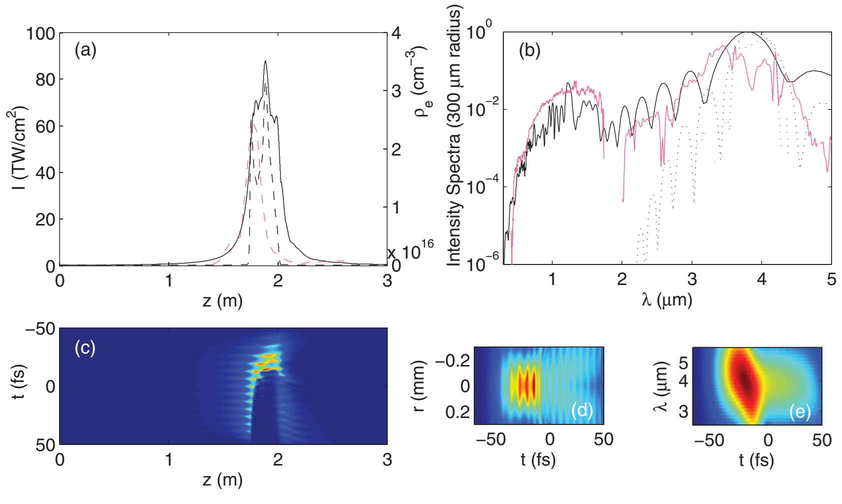

FIG. 6. (Color online) (a) Peak intensity (solid curve, left axis) and electron density (dashed curve, right axis) for the 3.9-μm pulse used in Ref. [9]. (b) Spectra averaged over a 300-μm-radius disk at $z = 0$ (black dotted curve) and $z = 2$ m (black solid curve). The pink (gray) curves recall the plasma and spectral data published in [9] (courtesy of D. Kartashov). Voltage data have been multiplied by a factor 2×10^{16}; spectral intensity values have been multiplied by a factor λ^2 at each wavelength. (c) Temporal dynamics in the (z,t) plane. (d) Compressed pulse profile at $z = 2$ m and (e) the corresponding XFROG trace.

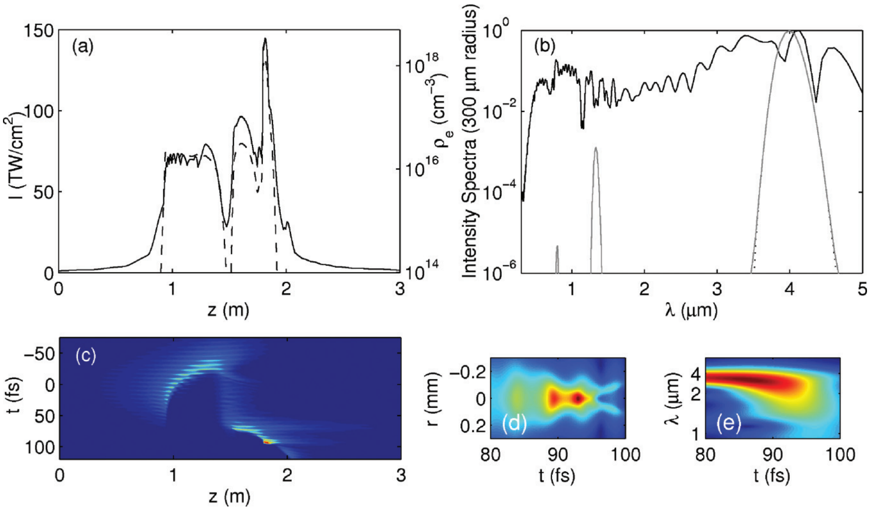

FIG. 7. (Color online) (a) Peak intensity (solid curve, left axis) and electron density (dashed curve, right axis) for a 80-fs, 3-mm-waisted, 4-μm Gaussian pulse focused with a $f = 1.5$ m lens. (b) Averaged spectra at $z = 0$ (dotted curve), $z = 2.5$ cm (gray solid curve), and $z = 1.9$ m (black solid curve). (c) Temporal dynamics in the (z,t) plane. (d) Optimally compressed pulse profile at $z = 1.9$ m and (e) the corresponding XFROG trace.

reproduce the observations reported in [9], in particular, the plasma length (~30 cm), about 4.8% maximum conversion around 1.2 μm, and a 3.4-octave spanning at the 10^{-4} level. Despite small differences, our model captures the essential physics underlying filament propagation and thus gives access to the inner pulse dynamics. Figures 6(c) and 6(d) reveal that only one focusing-defocusing event takes place near the linear focus, where the filament waist decreases to ~400–500 μm. Averaged over a circle of 300-μm radius around the filament core, the spectrum amplifies the third and fifth harmonics symmetrically before undergoing a limited blueshift at focus, which can be attributed to plasma generation. Figure 6(c) indeed confirms the poor influence of self-steepening in this configuration. Maximum compression remains limited to ~15.7 fs at focus, associated with an XFROG trace still centered at 4 μm [Figs. 6(d) and 6(e)].

By modifying the laser parameters and propagation geometry slightly, shorter light fields can be produced. Figure 7 indeed demonstrates that much higher compression rates can be achieved by keeping instead the setup chosen in Fig. 3 and only doubling the time extent of our Gaussian pulse with $t_p = 80$ fs. With an energy augmented to about 14 mJ and a shorter focal length ($f = 1.5$ m), the self-guiding range extends over 1 m with clamped intensity of ~100 TW/cm^2. During the filamentation process, the pulse lets the rear pulse refocus and develop a shock dynamics [Figs. 7(a) and 7(c)]. FWHM durations shrink between 7 fs ($z = 1.55$ m) and 5.5 fs ($z = 1.9$ m) due to strong self-steepening. Displayed in Fig. 7(b), the pulse similarly amplifies the third and fifth harmonics, but it forms at large distance a wider spectrum with a buildup of UV-visible wavelengths up to 10% conversion around 1 μm, achieving an almost four-octave spanning ($N = 3.83$). Figures 7(d) and 7(e) show that the intensity distribution at maximum compression is associated with the buildup of ~1-μm wavelengths. Note the strong chirp evidenced by the XFROG trace [Fig. 7(e)]. This suggests that even shorter pulse durations could be reached by using appropriate postcompression techniques.

VI. CONCLUSION

In summary, we have numerically examined the filamentation of femtosecond pulses propagating in different geometries at long central wavelengths up to 8 μm. Our major result is the possibility to reach very short (3–5 fs), energetic (~1 mJ) pulses along the filament range by using MIR wavelengths. In gases, short durations are connected with wide supercontinua in which four-wave mixing broadens the spectrum to long wavelengths and self-steepening amplifies the high-frequency part of the spectrum initiated by low-order harmonics. Self-compression is achieved in the part of the spectrum whose wavelengths are below the third harmonic of the carrier wave.

The standard filamentation model, which only relies on the dynamical balance between a cubic Kerr nonlinearity and the PPT ionization of gases, yields numerical results that do support the comparison with experimental measurements of MIR filaments. On this basis, we proposed a slight variant of the setup and laser parameters used in [9] to generate sub-10-fs pulses through the long-range self-channeling of MIR laser pulses.

ACKNOWLEDGMENTS

This work was performed using HPC resources from GENCI/CCRT/CINES (Grants No. 2012-x2012106003 and No. 2013-x2013057027). The authors thank Daniil Kartashov for providing them with the data of Fig. 1 of Ref. [9]. One of the authors (L.B.) thanks Stefan Skupin and Olga Kosareva for fruitful discussions.

---

[1] S. Skupin and L. Bergé, Opt. Commun. **280**, 173 (2007).
[2] L. Bergé, Opt. Express **16**, 21529 (2008).
[3] L. Bergé, C. L. Soulez, C. Köhler, and S. Skupin, Appl. Phys. B **103**, 563 (2011).
[4] B. Shim, S. E. Schrauth, and A. L. Gaeta, Opt. Express **19**, 9118 (2011).
[5] A. A. Voronin, S. Ališauskas, O. D. Mücke, A. Pugžlys, A. Baltuška, and A. M. Zheltikov, Phys. Rev. A **84**, 023832 (2011).
[6] T. Fuji and T. Suzuki, Opt. Lett. **32**, 3330 (2007).
[7] O. Chalus, A. Thai, P. K. Bates, and J. Biegert, Opt. Lett. **35**, 3204 (2010).

[8] G. Andriukaitis, T. Balčiunas, S. Ališauskas, A. Pugžlys, A. Baltuška, T. Popmintchev, M.-C. Chen, M. M. Murnane, and H. C. Kapteyn, Opt. Lett. **36**, 2755 (2011).

[9] D. Kartashov, S. Ališauskas, A. Pugžlys, A. Voronin, A. Zheltikov, M. Petrarca, P. Béjot, J. Kasparian, J. P. Wolf, and A. Baltuška, Opt. Lett. **37**, 3456 (2012).

[10] F. Silva, D. R. Austin, A. Thai, M. Baudisch, M. Hemmer, D. Faccio, A. Couairon, and J. Biegert, Nat. Commun. **3**, 807 (2012).

[11] W.-M. Wang, S. Kawata, Z.-M. Sheng, Y.-T. Li, L.-M. Chen, L.-J. Qian, and J. Zhang, Opt. Lett. **36**, 2608 (2011).

[12] T. Popmintchev, M. C. Chen, P. Arpin, M. M. Murnane, and H. C. Kapteyn, Nat. Photonics **4**, 822 (2010).

[13] L. Bergé, S. Skupin, C. Köhler, I. Babushkin, and J. Herrmann, Phys. Rev. Lett. **110**, 073901 (2013).

[14] J. Tate, T. Auguste, H. G. Muller, P. Salières, P. Agostini, and L. F. DiMauro, Phys. Rev. Lett. **98**, 013901 (2007).

[15] T. Popmintchev, M. C. Chen, D. Popmintchev, P. Arpin, S. Brown, S. Ališauskas, G. Andriukaitis, T. Balčiunas, O. D. Mücke, A. Pugžlys *et al.*, Science **336**, 1287 (2012).

[16] A. V. Husakou and J. Herrmann, Phys. Rev. Lett. **87**, 203901 (2001).

[17] M. Kolesik and J. V. Moloney, Phys. Rev. E **70**, 036604 (2004).

[18] L. Bergé, S. Skupin, R. Nuter, J. Kasparian, and J. P. Wolf, Rep. Prog. Phys. **70**, 1633 (2007).

[19] A. Dalgarno and A. E. Kingston, Proc. R. Soc. London, Ser. A **259**, 424 (1960).

[20] A. M. Perelomov, V. S. Popov, and M. V. Terent'ev, Sov. Phys. JETP **23**, 924 (1966).

[21] S. Skupin, G. Stibenz, L. Bergé, F. Lederer, T. Sokollik, M. Schnürer, N. Zhavoronkov, and G. Steinmeyer, Phys. Rev. E **74**, 056604 (2006).

[22] V. Loriot, E. Hertz, O. Faucher, and B. Lavorel, Opt. Express **17**, 13429 (2009).

[23] V. Loriot, E. Hertz, O. Faucher, and B. Lavorel, Opt. Express **18**, 3011 (2010).

[24] W. Ettoumi, Y. Petit, J. Kasparian, and J. P. Wolf, Opt. Express **18**, 6613 (2010).

[25] L. Bergé and J. J. Rasmussen, Phys. Plasmas **3**, 824 (1996).

[26] V. A. Andreeva, N. A. Panov, O. G. Kosareva, and S. L. Chin, Proc. SPIE **8512**, 85120Z (2012).

[27] G. P. Agrawal, *Nonlinear Fiber Optics*, 3rd ed. (Academic, San Diego, 2001).

[28] F. Théberge, N. Aközbek, W. Liu, A. Becker, and S. L. Chin, Phys. Rev. Lett. **97**, 023904 (2006).

[29] L. Bergé and S. Skupin, Phys. Rev. Lett. **100**, 113902 (2008).

[30] A. Vinçotte and L. Bergé, Phys. Rev. A **70**, 061802(R) (2004).